Supplemental Material for:

"Co-existence of Bloch and Néel walls in a collinear antiferromagnet"

M. S. Wörnle[1,2], P. Welter[1], M. Giraldo[2], T. Lottermoser[2], M. Fiebig[2], P. Gambardella[2], and C. L. Degen[1]

[1] *Department of Physics, ETH Zurich, Switzerland.*
[2] *Department of Materials, ETH Zurich, Switzerland.*

1. MATERIALS AND METHODS

1.1. Sample preparation

We study Cr_2O_3 domain walls on three bulk single crystals. Samples A and B (Refs. 1–3) are grown by the Verneuil method and oriented using a single-crystal X-ray diffractometer. The samples are cut perpendicular to the z-axis or (001) orientation. Subsequently, the samples are thinned down to 70 μm. Both samples are lapped and polished, each of them following a different process. Sample A is lapped using SiC powder with 3 μm grain size on a cast-iron-lapping plate. Subsequently, the sample is polished following a two-step process. In the first step, the lapped surface is polished with a soft metal plate using diamond powder with 1 μm grain size. In the second step, a refining polishing step follows using a polyurethane polishing plate together with colloidal silicate. Here, scratches from previous mechanical treatments are removed. The sample surface is polished until it reveals a root-mean-square (rms) roughness below 1 nm. Sample B is lapped using Al_2O_3 powder and H_2O solution. Next, the lapped surface is diamond polished until it reveals a surface with a rms roughness below 3 nm. Sample C (Ref. 3) is a flux-grown (001) Cr_2O_3 platelet of 30 μm thickness. The flat as-grown surface presents a rms roughness below 0.5 nm. SHG images of all crystals are shown in Figs. S1 and S2. We create antiferromagnetic domains by cooling samples through the transition temperature T_N. For samples A and B, domains are induced by magnetoelectric poling [4]. In sample C, different domain patterns spontaneously form when the sample is cooled through T_N.

1.2. Second harmonic generation (SHG) measurements

SHG microscopy exploits an interference contrast of frequency-doubled optical photons in domains of opposite magnetic polarization to reveal the domain pattern [1]. A magnetic contribution to the frequency-doubled light wave coupling linearly to the antiferromagnetic order parameter $\pm L$ interferes with a frequency-doubled crystallographic background contribution which identifies the two antiferromagnetic domain states by their different brightness [5]. We use a transmission SHG setup to acquire the SHG images, in which we use a Coherent Elite Duo laser system, which emits 120 fs pulses at a repetition rate of 1 kHz. An optical parametric amplifier tunes the wavelength to excite the bulk Cr_2O_3 samples with a photon energy of 1.033 eV and a pulsed energy of 80 μJ. The crystals are excited in transmission and at normal incidence by an unfocused circularly-polarized laser beam. Right-handed circularly-polarized light denote the clockwise rotation of the electric-field vector of light with respect to its propagation direction. The opposite follows for left-handed circular polarization. A camera lens is used to collect the SHG signal. Optical filters are added to select the SHG spectral wavelength, suppressing the fundamental beam and higher-harmonic contributions. SHG light is detected at room temperature with a Jobin-Yvon, back-illuminated, deep-depletion digital camera with a near-infrared detector chip of 1024×256 pixels. The camera is cooled with liquid nitrogen to reduce thermal noise.

1.3. Nanoscale scanning diamond magnetometry (NSDM) measurements

Scanning NV magnetometry measurements are carried out on a user-facility instrument, built in-house [6], and under ambient conditions. The instrument uses 520 nm laser light and 2.76 GHz to 2.91 GHz microwave pulses to detect the NV center spin resonances. Laser illumination is kept below 20 μW to avoid laser-induced heating of the sample. The spin resonance frequency is determined by sweeping the microwave frequency and fitting a Lorentzian function to the optically-detected magnetic resonance spectrum. Four different diamond probes (QZabre LLC) of $\sim 22\%$ CW ODMR contrast at a measurement count rate of ~ 200 kC/s are used. The sensitivity of these probes (as determined from the average least-squares variance of the center frequency) is 1.7 μT for an integration time of 6.4 seconds per pixel. All scans are performed on the Cr_2O_3 surface pointing towards the camera in the SHG experiment.

We use both continuous and pulsed ODMR protocols [7, 8] on either transition ($m_S = 0$ to $m_S = \pm 1$) of the NV center. A small external bias field of ~ 4 mT is applied to split the spin resonances; this small bias field is not expected to influence the Cr_2O_3 physics. To convert the measured spin resonance frequency f to units of magnetic field, we compute

$$B_{\mathrm{NV}} = \frac{f_0 - f}{28.02\,\mathrm{MHz/mT}} \tag{1}$$

where f_0 is the mean frequency taken over the entire scan, which is approximately the frequency far from the sample surface. We recall that NV magnetometry provides one vector component of the magnetic field, $B_{\mathrm{NV}} = \vec{e} \cdot \vec{B}$, which is the projection of $\vec{B}$ onto the anisotropy axis $\vec{e} = (e_x, e_y, e_z)$ of the spin. The unit vector $\vec{e} = (\sin\theta_{\mathrm{NV}} \cos\phi_{\mathrm{NV}}, \sin\theta_{\mathrm{NV}} \sin\phi_{\mathrm{NV}}, \cos\theta_{\mathrm{NV}})$ corresponds to the symmetry axis (N-V axis) of the NV center, as expressed by the laboratory frame angles θ_{NV} and ϕ_{NV}. The sensor vector orientation is pre-determined for each tip using an external field sweep. The stand-off distance z between NV center and the sample surface is measured by independent calibration scans over a magnetized Co stripe before and after the Cr_2O_3 scans [9, 10]. For our probes, $(\theta_{\mathrm{NV}}, \phi_{\mathrm{NV}}, z)$ is (55°, 270°, 73 ± 7 nm) for tip A, (55°, 180°, 64 ± 4 nm) for tip B, (55°, 176°, 65 ± 3 nm) for tip C and (55°, 176°, 68 ± 8 nm) for tip D.

2. DATA ANALYSIS

2.1. Effective surface magnetization σ_z^0

Antiferromagnetic order in the form of vertically alternating layers of oppositely polarized ions leads to an effective surface layer magnetization on the top and bottom surfaces of the crystal, in analogy to the bound surface charge appearing for a polarized dielectric [11–13]. To calculate the surface magnetization, we assign the alternating layers of opposite polarization to two oppositely magnetized volumes, each with magnetization $M_s = nm/V$, vertically shifted with respect to each other by s. Here, n is the number of ions per unit cell and polarization direction, m is the magnetic moment per ion, and V is the volume of the unit cell. Within the bulk, the magnetization of the two volumes is exactly compensated, except in two thin layers of thickness s at the top and bottom

of the body. Thus, the bulk antiferromagnetic order appears like an magnetized surface layer at the top and bottom of the crystal, with an effective layer magnetization of

$$\sigma_z^0 = dM_s = \frac{nms}{V} \ . \tag{2}$$

For thick crystals a local magnetic probe only detects the stray field of the top layer.

Cr_2O_3 has a hexagonal unit cell with a lattice constant of $a_{\mathrm{hex}} = 4.96\,\text{Å}$, corresponding to a side length of $a/\sqrt{3} = 2.86\,\text{Å}$, a height of $c = 13.6\,\text{Å}$, a hexagonal surface area of $A = \frac{3\sqrt{3}}{2}a^2 = 21.3\,\text{Å}^2$, and a volume of $V = Ac = 290\,\text{Å}^3$ (Refs. 3 and 13). The hexagonal unit cell is constructed from six vertically stacked O^{2-} planes. Each O^{2-} plane has two nearest Cr^{3+} ions of opposite magnetic polarization located 0.941 Å above or below the plane, respectively, therefore $s = 1.88\,\text{Å}$ (see Fig. 2a and Ref. 3). Accounting for the 12 Cr^{3+} ions per unit cell, $n = 6$ for each orientation. Assuming a moment of $m = 2.8\,\mu_\mathrm{B}$ per Cr^{3+} ion [14], we calculate a surface magnetization of

$$\sigma_z^0 = \frac{6 \times 2.8\,\mu_\mathrm{B} \times 0.188\,\text{nm}}{0.290\,\text{nm}^3} = 10.9\,\mu_\mathrm{B}/\text{nm}^2 \ . \tag{3}$$

This is slightly less than what one would expect from one monolayer of Cr^{3+} ions, which would have a magnetization of $m/A = 12.1\,\mu_\mathrm{B}/\text{nm}^2$.

2.2. Transformations between surface magnetization and magnetic field

Using the relations between magnetization and magnetic stray field for two-dimensional thin films [15], we can reconstruct the surface magnetization $\sigma_z(x, y)$ and vector magnetic field $\vec{B}(x, y)$ from the measured stray field component $B_{\mathrm{NV}}(x, y)$. We perform transformations in Fourier space. The magnetic vector field $\vec{B}$ associated with the magnetization $\vec{\sigma}$ is given by

$$\left(\hat{B}_x, \hat{B}_y, \hat{B}_z\right) = \frac{1}{2}\mu_0 e^{-kz}\left(-k_x\hat{\sigma}_k - ik_x\hat{\sigma}_z, -k_y\hat{\sigma}_k - ik_y\hat{\sigma}_z, -ik\hat{\sigma}_k + k\hat{\sigma}_z\right) \tag{4}$$

where k_x, k_y are the in-plane k-vectors, $k = (k_x^2 + k_y^2)^{1/2}$, $\hat{\sigma}_k = (k_x\hat{\sigma}_x + k_y\hat{\sigma}_y)/k$, and hat symbols denote Fourier transforms in x and y. z is the stand-off distance of the sensor and $\mu_0 = 4\pi \times 10^{-7}\,\text{Tm/A}$. For a line scan in x direction, scanned across a domain wall extending in y direction, the magnetic field is

$$\left(\hat{B}_x, \hat{B}_y, \hat{B}_z\right) = \frac{1}{2}\mu_0 e^{-kz}\left(-k_x\hat{\sigma}_x - ik_x\hat{\sigma}_z, 0, -ik\hat{\sigma}_x + k\hat{\sigma}_z\right) \ , \tag{5}$$

where now $k = |k_x|$. Likewise, we can recover the magnetic vector field $\vec{B}$ from the measured projection B_{NV} as

$$\left(\hat{B}_x, \hat{B}_y, \hat{B}_z\right) = \frac{1}{k_{\mathrm{NV}}}\left(ik_x, ik_y, -k\right)\hat{B}_{\mathrm{NV}} \tag{6}$$

where $k_{\mathrm{NV}} = (ie_xk_x + ie_yk_y - e_zk)$ and (e_x, e_y, e_z) is the vector orientation of the sensor. Finally, under the assumption that the magnetization is fully out-of-plane ($\sigma_x = \sigma_y = 0$), we can reconstruct σ_z from the stray field B_{NV},

$$\hat{\sigma}_z = -\frac{2W\hat{B}_{\mathrm{NV}}}{\mu_0 e^{-kz}k_{\mathrm{NV}}} \tag{7}$$

where $W = W(k)$ is a suitable window function (here a Hann function) that provides a high-frequency cutoff. Although our Cr_2O_3 films do have an in-plane component in the vicinity of the domain wall, the reconstructed σ_z still accurately reproduces the domain pattern and surface magnetization σ_z^0.

2.3. Magnetic field from surface roughness

Surface roughness leads to tiny stray fields at topographic steps, as sketched in Fig. 1b. The magnetic field produced at a step of height h corresponds to the differential field of two magnetized layers located at z and $z + h$. According to Eq. 5, the B_z field of the step is given by

$$\hat{B}_z = \frac{1}{2}\mu_0 e^{-kz} kh(k\hat{\sigma}_z) \ . \tag{8}$$

For a simple order-of-magnitude estimate of the stray field, we look at the Fourier component of σ_z that produces the strongest B_z. This occurs for $k = 2/z$. For this Fourier component, the amplitude of B_z is

$$B_z = \frac{\mu_0 h 2e^{-2}\sigma_z^0}{z^2} \approx \frac{0.2707\mu_0 h\sigma_z^0}{z^2} \tag{9}$$

For our Cr_2O_3 crystals, where $\sigma_z^0 \approx 2\,\mu_B/\mathrm{nm}^2$, and using $z = 68\,\mathrm{nm}$, we find $B_z/h \approx 1.4\ \mu\mathrm{T/nm}$. For an rms surface roughness of 3 nm-rms we therefore expect stray field fluctuations of $\sim 5\ \mu\mathrm{T}$, in good agreement with the experimental 7 μT-rms (Fig. 2d).

2.4. Fitting of line scans

We model the domain wall as presented in Eq. 1 in the main text. The stray field is then computed via Eq. 5. The resulting model features 7 parameters: the effective surface magnetization σ_z^0, the position of the domain wall x_0, its width parameter Δ and twist angle χ, and the sensor geometry $(z, \theta_{\mathrm{NV}}, \phi_{\mathrm{NV}})$. Since z, θ_{NV}, ϕ_{NV} have been determined separately at this point, they are left fixed in the following least-squares optimization, leaving only σ_z, x_0, Δ and χ as free parameters.

The initial value of σ_z^0 is determined by estimating the surface magnetization using the two complementary methods (step height, integration of B_x) described below. The initial value for width and chirality are set to $\Delta = 40\,\mathrm{nm}$ and $\chi = 90°$. We checked that other starting values did not significantly alter the fit results. The fitting procedure is repeated for each individual line scan.

2.5. Complementary methods for estimating σ_z^0

We use two complementary methods for estimating the Cr_2O_3 surface magnetization σ_z^0 from a stray field scans across domain walls:

Step height in reconstructed σ_z map: We reconstruct the surface magnetization $\sigma_z(s)$ using Eqs. (5) and (7). The step height at the domain wall is $2\sigma_z^0$.

Integration of B_x: We assume a domain wall extending along the y direction. We compute the $B_x(x)$ component of the stray field from $B_{\mathrm{NV}}(x)$, using the known orientation of the sensor $(\theta_{\mathrm{NV}}, \phi_{\mathrm{NV}})$ and Eq. (6). The integrated $B_x(x)$ is then equal to $\mu_0\sigma_z^0$, irrespective of the stand-off z and the domain-wall profile and chirality. To explain this, assume an out-of-plane magnetized film with magnetization $\vec{\sigma}(x')$ and a domain wall centered at $x = 0$ and extending along the y-direction. The step edge can have a σ_x or σ_y component. The magnetic field B_x produced by the magnetization element $\mathrm{d}x'\vec{\sigma}(x')$ is

$$\mathrm{d}B(x) = \frac{\mu_0 j_y(x')t\mathrm{d}x'z}{2\pi[(x-x')^2+z^2]} \tag{10}$$

where $j_y(x')t = [\vec{\nabla}\times\vec{\sigma}]_y(x') = -[\partial_x\sigma_z](x')$ is the bound current element associated with $\vec{\sigma}(x')$ and t is the film thickness ($t \ll z$). The total magnetic field at position x is

$$B(x) = \int_{-\infty}^{\infty}\mathrm{d}x'\frac{\mu_0 j_y(x')tz}{2\pi[(x-x')^2+z^2]} = -\int_{-\infty}^{\infty}\mathrm{d}x'\frac{\mu_0 z}{2\pi[(x-x')^2+z^2]}\,[\partial_x\sigma_z](x') \tag{11}$$

and the integrated $B(x)$ is

$$\int_{-\infty}^{\infty}\mathrm{d}xB(x) = -\left(\int_{-\infty}^{\infty}\mathrm{d}x''\frac{\mu_0 z}{2\pi[(x'')^2+z^2]}\right)\left(\int_{-\infty}^{\infty}\mathrm{d}x'[\partial_x\sigma_z](x')\right) \tag{12}$$

$$= -\frac{\mu_0}{2}\left[\sigma_z(+\infty)-\sigma_z(-\infty)\right] = \mu_0\sigma_z^0 \tag{13}$$

where we have used Fubini's theorem and the last equation is for a domain wall where $[\sigma_z(+\infty) - \sigma_z(-\infty)] = -2\sigma_z^0$.

2.6. Complementary method for estimating Δ and χ

For a fixed pair (χ,Δ), we only fit x_0 to the data, and record the residual sum of squares (RSS). The surface magnetization is determined for each line scan by the previously introduced three complementary methods. The RSS is a measure of the likelihood. Indeed, assuming Gaussian errors, the log-likelihood is given by

$$\ln\mathcal{L} = \ln\left(\frac{1}{2\pi\sigma^2}\right)\frac{n}{2} - \frac{1}{2\sigma^2}\mathrm{RSS} \tag{14}$$

Here, σ is the standard deviation describing the error of a single data point, and n is the number of data points. We can compare the relative likelihood of two models 1 and 2 (*i.e.* two pairs of Δ and χ) by estimating $\sigma_i^2 = \mathrm{RSS}_i/n$, $i \in \{1,2\}$, giving

$$\ln\mathcal{L}_1 - \ln\mathcal{L}_2 = -\frac{n}{2}\ln\frac{\mathrm{RSS}_1}{\mathrm{RSS}_2} \tag{15}$$

We choose model 2 as the best model (i.e. the least squares solution), so that Eq. 15 is normalized to 0. To consider the data from all scans, we sum the RSS of each line and scan, and set n to be the total number of data points.

3. SUPPLEMENTARY FIGURES

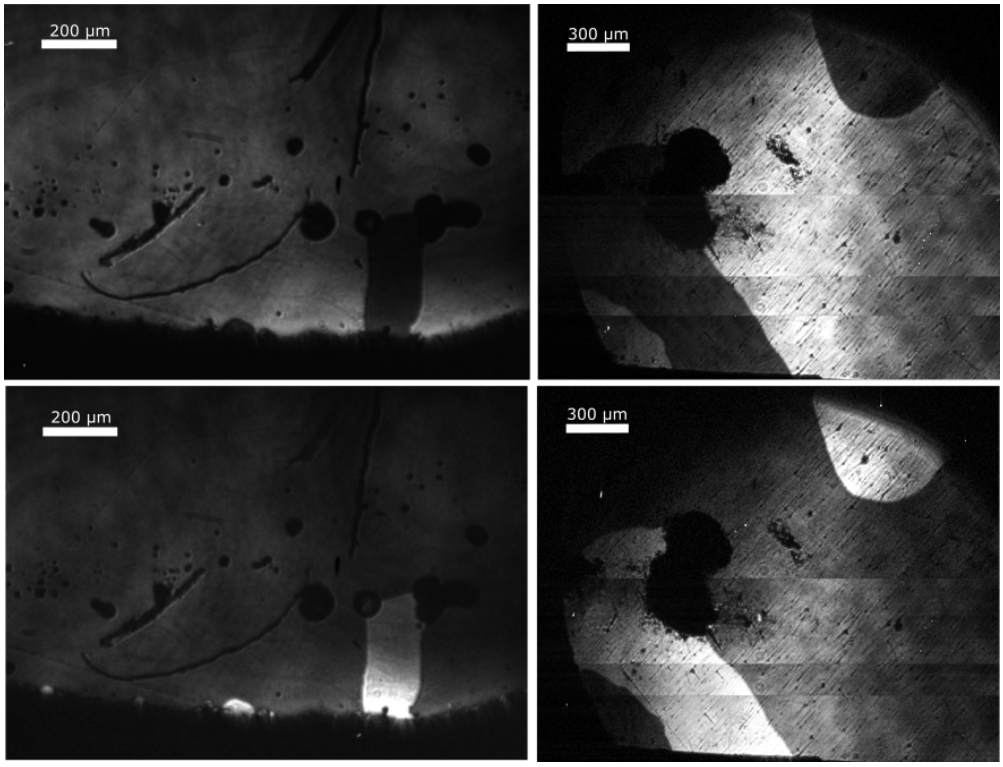

Fig. S1. SHG microscopy images of sample A (left panels) and sample B (right panels). Upper panels used left-handed circular polarization, lower panels used right-handed circular polarization.

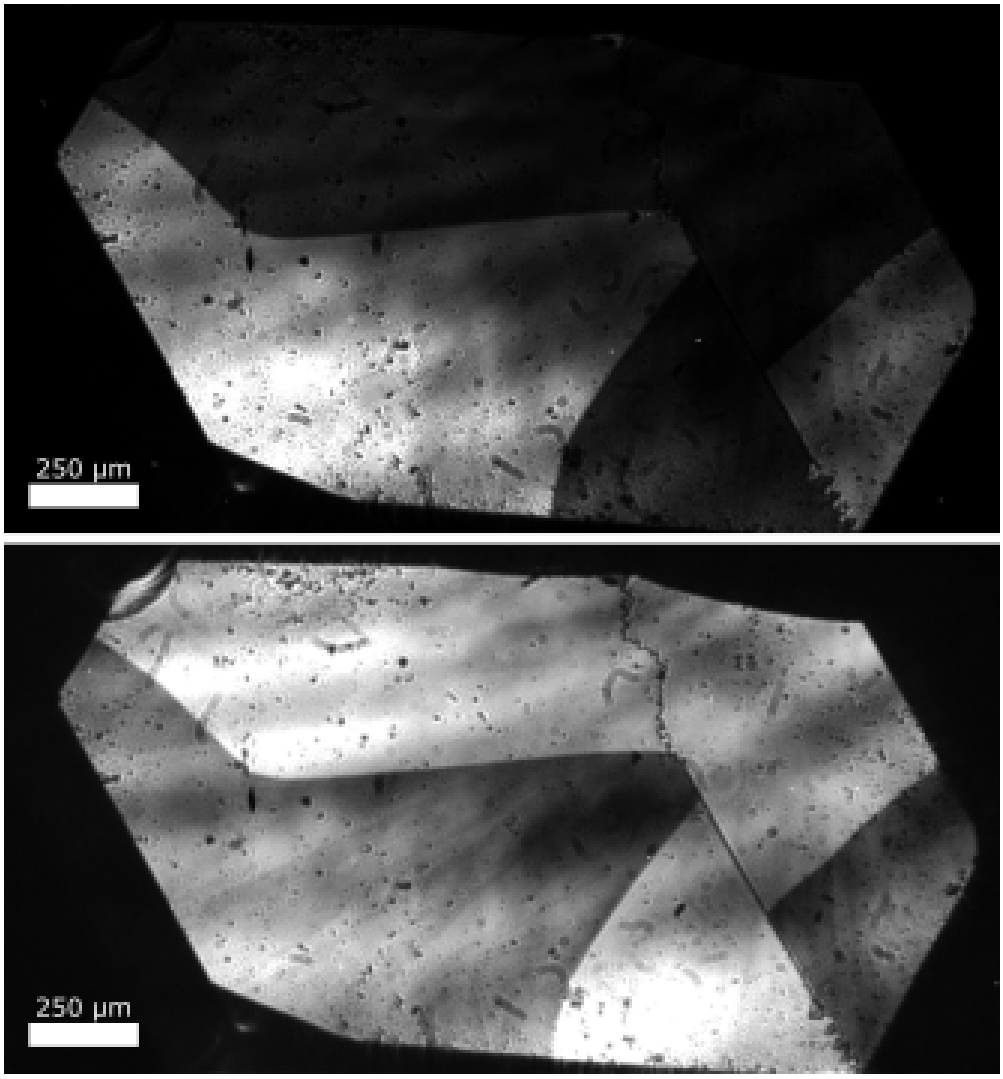

Fig. S2. SHG microscopy images of sample C. Upper panel used left-handed circular polarization, lower panel used right-handed circular polarization.

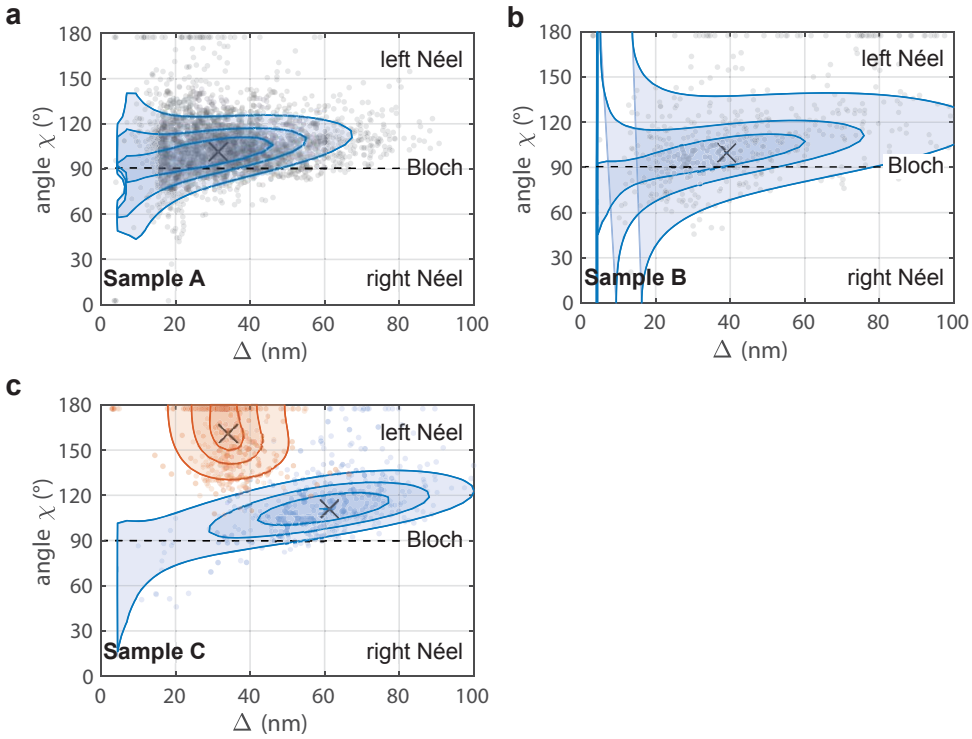

Fig. S3. Maximum likelihood estimates for domain wall width Δ and twist angle χ, as explained in the Methods section. Gray dots are fit results from individual line scans. Colored contours are maximum likelihood isolines containing 75%, 50%, and 25% of datapoints. The most likely (χ, Δ) pair is indicated by a central cross. For sample C, datasets with $\alpha > 9°$ (blue) and $\alpha < 9°$ (red) are analyzed separately.

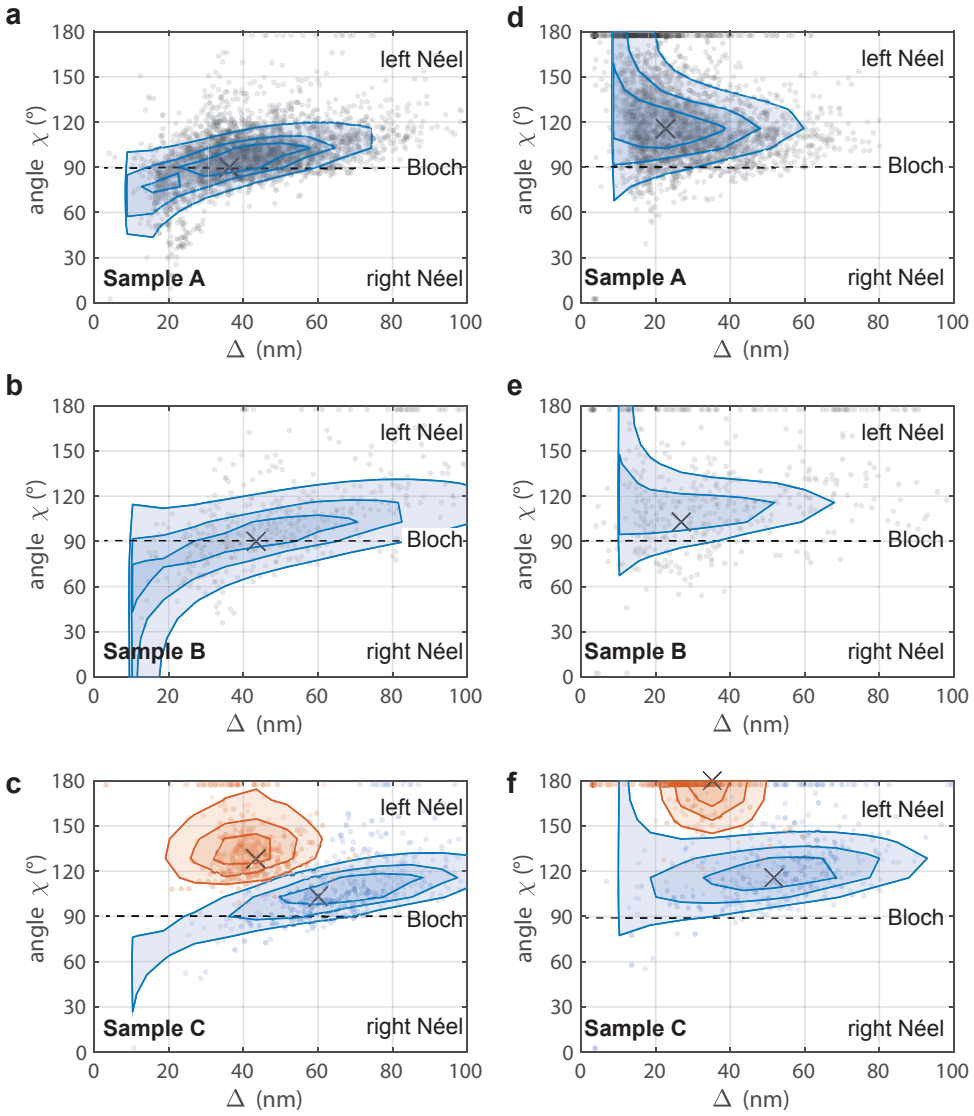

Fig. S4. Maximum likelihood estimates for domain wall width Δ and twist angle χ for upper and lower bound stand-off distances $z \pm 10\,\mathrm{nm}$, where z is the calibrated stand-off distance. **a-c** Maximum likelihood estimates for the lower bound $z - 10\,\mathrm{nm}$. **d-f** Maximum likelihood estimates for the upper bound $z + 10\,\mathrm{nm}$. Data points, contours and central cross are as with Fig. S3. We note that the our observation – the presence of Bloch-like walls in samples A and B, and mixed Bloch and Néel walls in sample C – is valid within the uncertainty of the sample-sensor distance. The $z \pm 10\,\mathrm{nm}$ bounds are a conservative estimate, as all probes showed a calibration error of $\leq 8\,\mathrm{nm}$ (see Methods).

[1] M. Fiebig, D. Fröhlich, G. Sluyterman v. L., and R. V. Pisarev, Domain topography of antiferromagnetic Cr_2O_3 by second-harmonic generation, Applied Physics Letters **66**, 2906 (1995).

[2] M. Fiebig, D. Fröhlich, and H. J. Thiele, Determination of spin direction in the spin-flop phase of Cr_2O_3, Phys. Rev. B **54**, R12681 (1996).

[3] M. Fiebig, Nichtlineare spektroskopie und topografie an antiferromagnetischen domänen, PhD Thesis (1996).

[4] B. B. Krichevtsov, V. V. Pavlov, and R. V. Pisarev, Nonreciprocal optical effects in antiferromagnetic Cr_2O_3 subjected to electric and magnetic fields, Sov. Phys. JETP **67**, 378 (1988).

[5] M. Fiebig, D. Fröhlich, B. B. Krichevtsov, and R. V. Pisarev, Second harmonic generation and magnetic-dipole-electric-dipole interference in antiferromagnetic Cr_2O_3, Phys. Rev. Lett. **73**, 2127 (1994).

[6] https://spin.ethz.ch/quantum-technology/nsdm.html, https://spin.ethz.ch/quantum-technology/nsdm.html, retrieved on 2020-08-20 (2020).

[7] A. Dréau, M. Lesik, L. Rondin, P. Spinicelli, O. Arcizet, J. F. Roch, and V. Jacques, Avoiding power broadening in optically detected magnetic resonance of single NV defects for enhanced dc magnetic field sensitivity, Phys. Rev. B **84**, 195204 (2011).

[8] R. Schirhagl, K. Chang, M. Loretz, and C. L. Degen, Nitrogen-vacancy centers in diamond: Nanoscale sensors for physics and biology, Annu. Rev. Phys. Chem. **65**, 83 (2014).

[9] J. P. Tétienne, T. Hingant, L. J. Martinez, S. Rohart, A. Thiaville, L. H. Diez, K. Garcia, J. P. Adam, J. V. Kim, J. F. Roch, I. M. Miron, G. Gaudin, L. Vila, B. Ocker, D. Ravelosona, and V. Jacques, The nature of domain walls in ultrathin ferromagnets revealed by scanning nanomagnetometry, Nat. Commun. **6**, 6733 (2015).

[10] S. Vélez, J. Schaab, M. S. Wörnle, M. Müller, E. Gradauskaite, P. Welter, C. Gutgsell, C. Nistor, C. L. Degen, M. Trassin, M. Fiebig, and P. Gambardella, High-speed domain wall racetracks in a magnetic insulator, Nature Communications **10**, 4750 (2019).

[11] K. D. Belashchenko, Equilibrium magnetization at the boundary of a magnetoelectric antiferromagnet, Phys. Rev. Lett. **105**, 147204 (2010).

[12] A. Andreev, Macroscopic magnetic fields of antiferromagnets, Journal of Experimental and Theoretical Physics Letters **63**, 758 (1996).

[13] X. He, Y. Wang, N. Wu, A. N. Caruso, E. Vescovo, K. D. Belashchenko, P. A. Dowben, and C. Binek, Robust isothermal electric control of exchange bias at room temperature, Nature Materials **9**, 579 (2010).

[14] O. Madelung, U. Rössler, and M. S. (ed.), Chromium sesquioxide (Cr_2O_3): magnetic properties, In: Non-Tetrahedrally Bonded Binary Compounds II (Springer, Berlin-Heidelberg, 2000) .

[15] I. A. Beardsley, Reconstruction of the magnetization in a thin film by a combination of lorentz microscopy and external field measurements, IEEE Transactions on Magnetics **25**, 671 (1989).